Direct Look at the Electric Field in Ketosteroid Isomerase and its Variants

Matthew R. Hennefarth† and Anastassia N. Alexandrova*,†,‡

†*Department of Chemistry and Biochemistry, University of California, Los Angeles, 607 Charles E. Young Drive East, Los Angeles, CA 90095-1569, USA*

‡*California NanoSystems Institute, University of California, Los Angeles, 570 Westwood Plaza, Los Angeles, California 90095-1569, USA*

E-mail: *ana@chem.ucla.edu

Phone: +1 310 825-3769

Abstract

Enzymes catalyze a number of reactions with high efficiency and stereoselectivity. It is thought that strong, direct, and permanent electric fields within the active site of the enzyme contribute to the superb catalytic efficiency of enzymes. This effect is called electrostatic preorganization. Most often, electrostatic preorganization is analyzed by evaluating the local electric field at discrete points, such as a bond center, using, for example, vibrational Stark spectroscopy. However, the protein macromolecule creates a significantly more complicated heterogeneous electric field that affects the entire active site, whose total change density thus gets perturbed, with the implications for the catalytic mechanism. We present a global distribution of streamlines method to analyze the topology of the heterogeneous electric fields in within an enzyme active site. We focus on ketosteroid isomerase (KSI), an enzyme known to produce a field on the order of 100 MV/cm along the critical carbonyl bond in the steroid substrate. We investigate how mutations known to cause activity changes, as well as applied small external electric fields perturb the electric fields in the KSI active site. Where classical single-point analysis failed, using our method allowed us to properly correlate global changes in the electric field to changes in the reaction barrier. We were able to show that topologically similar local electric fields had similar reaction barriers.

Keywords

KSI, Electrostatic Preorganization, Electric Field, Vector Field, Enzymes

Enzymes are an essential part of biology, chemistry, and medicine. They can catalyze chemical reaction with incredible efficiency and stereoselectivity under physiological conditions, and thus are desirable tools for catalyzing non-native reactions in a wide variety of applications. While a protein can be comprised of several hundred amino acid residues, only a small subset of these residues actually interacts with the substrate during the reaction. This begs the question of the necessity of the rest of the protein scaffold for catalysis. It is hypothesized that the rest of the protein contributes to catalysis by producing a highly specific and preorganized electric field that facilitates the reaction.

The formation of this specific electric field falls within the idea of electrostatic preorganization, the notion that enzymes create an electrostatically organized environment such that there is a reduced entropic cost to reach the rate-determining transition state (TS).[1,2] If the reaction that a protein catalyzes would instead occur, for example, in a polar solvent, there would be an entropic penalty to realign the solvent's dipoles to stabilize the TS.[1,3] The free energy difference between the TS and reactant determines the reaction rate; therefore, lowering the free energy barrier by removing the entropic penalty to reach TS while simultaneously destabilizing the reactant state would greatly increase the reaction rate. It is thought that proper alignment of charged amino acid residues surrounding the active site, even at a distance, creates a permanent electric field that is optimized within the active site for the reaction. It has been shown that residues in the first and second coordination sphere contribute the most to this electric field.[4–7] Hence, the protein scaffold needs to be folded in a specific way such that these residues are in the correct spatial position and orientation to optimize the effect of the electric field on the active site.

It is of interest to be able to quantify a protein's electrostatic preorganization so to better understand the functionality of natural enzymes and to improve computationally designed enzymes, whose starting activity remains suboptimal.[8–12] One of the most studied enzymes in the context of understanding electrostatic preorganization is ketosteroid isomerase (KSI) (Figure 1). Subjected to both theoretical and experimental interrogations, KSI has one of the highest known unimolecular rate constants[13,14] with many theoretical[15–21] and experimental[22–26] studies investigating its electrostatic preorganization. KSI catalyzes the isomerization of a steroid by altering the position of a C=C double bond through formation of a charged enolate after a proton abstraction and reinserting the

proton two carbons away (Scheme 1). When the charged intermediate forms, there is expected to be an increased dipole along the carbonyl bond due to a resonance-assisted decrease of the double bond character.

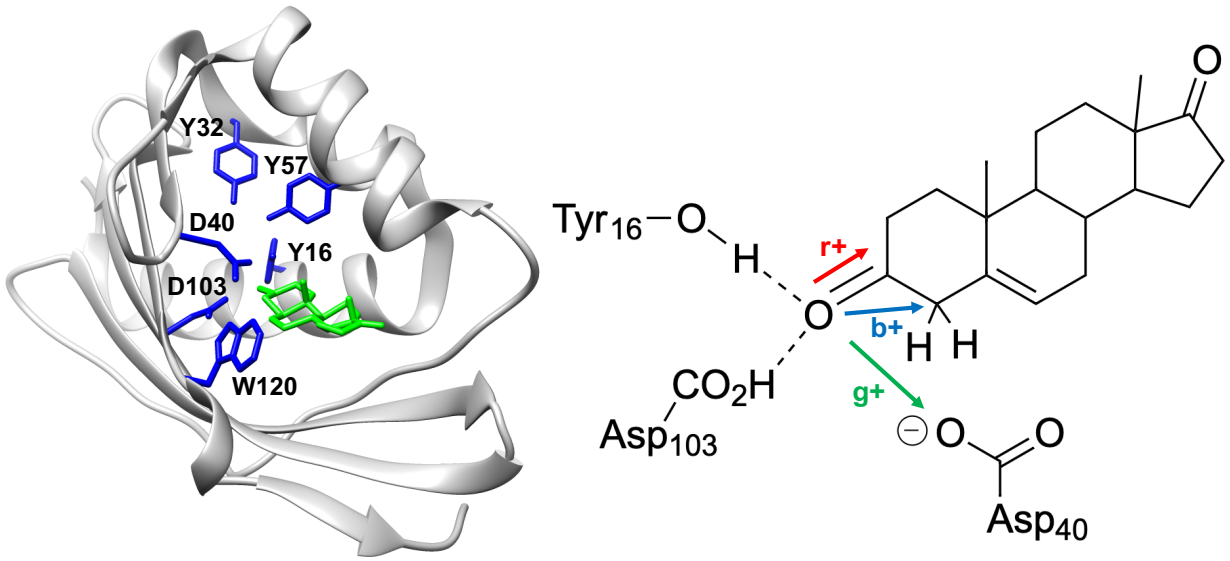

Figure 1: Full KSI protein (PDB code 1OH0[27]). Residues included in the small-scale calculations are highlighted in blue. The substrate is colored green. At right, the site is shown schematically, with red, blue, and green arrows representing the directions of the external electric fields applied to the system in this study.

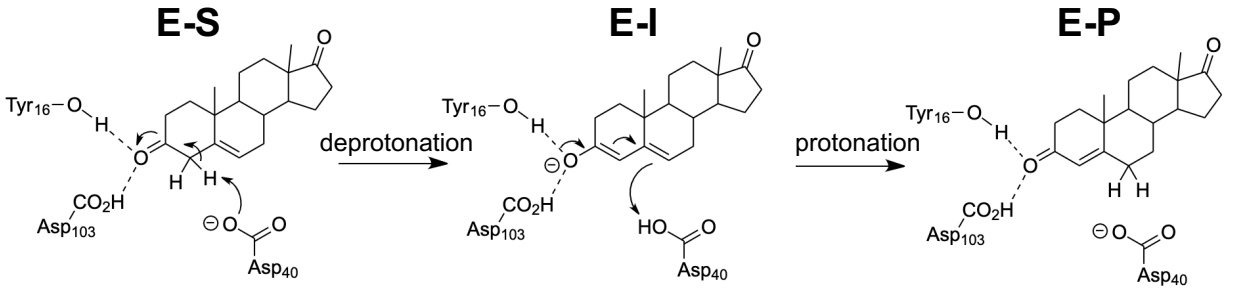

Scheme 1: Reaction catalyzed by KSI including important residues along the reaction pathway.

Warshel used the empirical valence bond (EVB) method to detect differing amounts of electrostatic preorganization depending on the confirmation of the substrate present in KSI;[15,18] he also used the same approach to explain the catalytic efficiency of methyltransferases.[28] Boxer later showed using vibrational Stark spectroscopy that KSI exerts an optimized electric field, around -144 ± 6 MV/cm, along the carbonyl bond to increase the stability of the first TS and the intermediate.[24] Calculations of the vibrational shifts of a nitrile probe in KSI confirmed the findings by Boxer.[17] Head-Gordon has used

molecular dynamic simulations to investigate the fluctuation of the electric field at the carbonyl bond in KSI throughout the catalytic cycle.[7] More recently, Sokalski has investigated the dynamic nature of the electric field and its role in proton dislocations in the hydrogen-bond network around the substrate carbonyl. In theoretical studies, the electric field is probed at only discrete points: either the center of the bond or at the two atoms that make up the bond in question. However, the electric field in the active site is heterogeneous and more complicated than what a single point can describe. At the same time, the electron density on the carbonyl is interdependent with the electron density in the rest of the active site. The entire electron density is affected by the heterogeneous electric field, which thus affects the catalyzed reaction. Previous studies have shown that external electric fields can significantly influence the reaction rates,[29–33] and molecular properties, including chemical bonds[34]. No theoretical or experimental method to date actually probes the full electric field in the region that makes up the carbonyl bond, or the full active site.

The electric field is dependent on both the electron density, $\rho(\mathbf{r})$, and nuclear coordinates. Under the assumption that the nuclear coordinates are relatively constant across systems we might be interested to compare, changes in $\rho(\mathbf{r})$ should reflect changes in $\mathbf{E}(\mathbf{r})$. Additionally, $\rho(\mathbf{r})$ is a scalar function, making it easier to analyze the global properties of $\rho(\mathbf{r})$. As such, the analysis of the topology of $\rho(\mathbf{r})$ through quantum theory of atoms in molecules (QTAIM) has also been utilized to explore electrostatic preorganization in KSI,[16] and in the histone deacetylase 8.[5] In these previous studies, we have shown that active site critical points of $\rho(\mathbf{r})$ as well as the curvature and charge density at these critical points are good descriptors of electrostatic preorganization.[5,16] Specifically for KSI, the QTAIM formalism was employed to detect changes in the topological properties of $\rho(\mathbf{r})$ as different uniform, external electric fields were applied to the active site of KSI. We showed how the changes in the QTAIM signature of the active site correlated strongly with both the electric field, and the changes in the reaction barrier of KSI. Therefore, $\rho(\mathbf{r})$ serves as a convenient scalar mediator between the reaction rate and the electric field, enabling an indirect analysis of the electrostatic preorganization. While analysis of $\rho(\mathbf{r})$ provides an indirect measurement of electrostatic preorganization, it still does not map or analyze the actual non-uniform vector electric field produced by the protein.

Traditional theoretical treatment of the electric vector field consists of evaluating the field at singular points, disregarding the general topology of the electric field.[4,7,21,35,36] Here, we introduce a method to quantify perturbations in the locally produced electric fields that incorporates the geometry of the electric field so as to directly quantify the electrostatic preorganization. We use KSI as a model system due to the large number of experimental and theoretical studies investigating its electrostatic preorganization. We showcase our method on two types of systems. In the first type, we apply external electric fields to the active site of KSI so as to decouple it from the heterogeneous effects of the protein residues; the field affects the reaction barrier. The second type are actual 3-chlorotyrosine mutants of KSI, which have been reported to cause changes in electrostatic preorganization and the reaction rate.[4,25]

We used the same small-scale active site of KSI (PDB Code 1OH0[27]) as in our previous study.[16] Residues to include (Figure 1) were chosen due to their proximity to the substrate as these have been shown to have the greatest contribution to the reaction barrier.[4] For each residue included, we cut the bond between the alpha and beta carbon and capped the beta carbon with a hydrogen. We then froze the cartesian coordinates of both the beta carbon and hydrogen. Previous studies have shown that the rest of the protein outside of the active site that we consider contributes an electric field only on the order of 10 MV/cm to the active site.[4,16] We additionally calculated the magnitude of the electric field of the protein at the positions of the substrate carbonyl carbon and oxygen, but with our active site removed. For this, we used the atomic charges on all atoms in the protein determined from the Atomic Charge Calculator II.[37] We find that the electric field magnitude is 13.7 MV/cm at the oxygen and 14.8 MV/cm at the carbon, in good agreement with previous estimations in Refs. 4 and 16. Optimized structures and reaction barriers for the active site of WT-KSI with and without a uniform external electric field were taken from our previous study.[16] Uniform electric fields of magnitude 10 MV/cm were applied one at a time to the system in the directions shown in Figure 1. These directions are along the carbonyl bond, from the carbonyl oxygen to the α-carbon, and from carbonyl oxygen to $Asp_{40}O$ (red, blue, and green arrows respectively). These systems are labeled $r+$, $r-$, $b+$, $b-$, $g+$, with + being the same and − the opposite direction of the arrow in the figure. The directions chosen are meant to

activate (+) and deactivate (-) the carbonyl (red arrow), and to generally facilitate (+) and inhibit (-) the deprotonation of the substrate (blue and green arrows).

Additionally, it has been shown that mutating tyrosines involved in the extended hydrogen bonding network surrounding the carbonyl oxygen (Y_{16}, Y_{32}, Y_{57}) to 3−chlorotyrosines can reduce the k_{cat} to 1/5 of that of the wildtype rate.[25,38] These residues were determined to produce the majority of the electric field in the KSI active site.[4] Hence, we also evaluated the reaction barrier and local electric field for Y_{32} and Y_{57} substituted with 3−chlorotyrosines without the presence of an external electric field (labeled KSI-Y^{32} and KSI-Y^{57}, respectively). The starting structures for 3−chlorotyrosines mutants came from the crystal structure (PDB code 5KP3[25]).

Reaction Barriers for 3-Chlorotyrosine Mutants and with External Fields

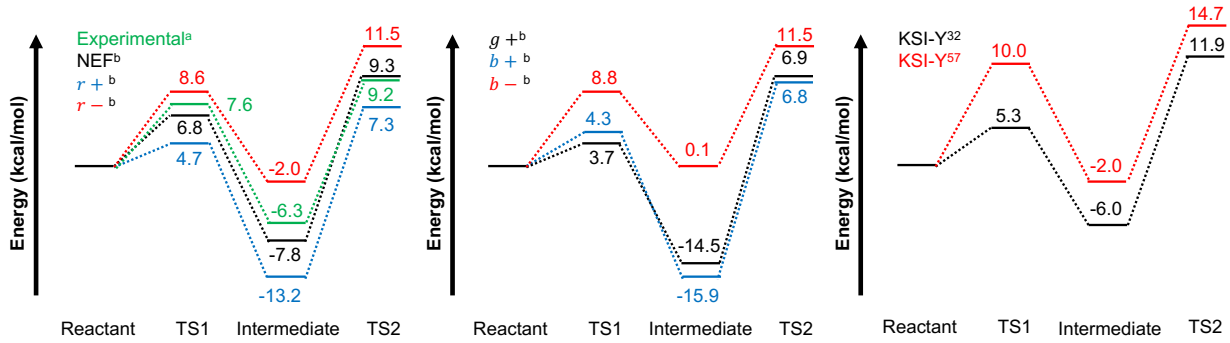

Figure 2: Reaction barriers for the KSI mutants and external electric field structures. Values shown are in kcal/mol. [a]Data for experimental values (green in far left) taken from Houck and Pollack.[20] [b]Data for theoretical values of barriers from external fields taken from Fuller et al.[16] The remaining barriers are calculated in this work. NEF: No external field.

Figure 2 summarizes the calculated electronic energy barriers for the 3−chlorotyrosine substituted structures (KSI-Y^{32} and KSI-Y^{57}) and the wild-type KSI structure with varying uniform, electric fields. We calculate a lower deprotonation barrier for KSI-Y^{32} and a higher deprotonation barrier for KSI-Y^{57} in comparison to the wild-type. Further, we calculate a slightly higher reprotonation barrier for KSI-Y^{32} and slightly lower reprotonation barrier for KSI-Y^{57}, relative to the intermediate state ($\Delta E_2^{\ddagger}$). Though, the transition state for reprotonation was higher in energy relative to the reactant state in comparison to the WT-KSI. Initial characterization of these 3−chlorotyrosine mutated KSI proteins determined experimentally that the overall reaction $\Delta\Delta G^{\ddagger}$ from KSI-WT was 0.34 kcal/mol for KSI-Y^{32}

and 0.94 kcal/mol for KSI-Y^{57}.[25] Note that our calculated barriers only consider the difference in electronic energy and is an approximation to the actual free energy barrier. Overall, our results agree qualitatively with that of the experiment that there are considerable changes in the barrier, though there are no experimental studies that decomposes the enthalpy terms from the reaction barrier for these mutants to compare quantitatively. Note that the idea of electrostatic preorganization rests on the notion that entropy being minimized during the reaction step, which is a justification for our focus on the enthalpies. In addition, we assume that the electric field should really be dependent on the electronic energy only. This is because the electric field that we compute (Equation 1) is dependent on $\rho(\mathbf{r})$.

Addition of a Cl at the ortho-position, relative to the oxygen, creates an inductive effect that lowers the pK_a of tyrosine by 1.8 units.[38] Previous studies on the 3−chlorotyrosine KSI mutated structures have shown that KSI-Y^{57} directly impacts the hydrogen bond between Y_{16} and the substrate carbonyl.[25,38] KSI-Y^{32} changes the orientation of Y_{57} relative to Y_{16} and thus imparts a smaller effect on the reaction barrier. These mutations do not affect the folding or crystal structure of the protein very much, and hence should have a minimal perturbation to residue placement. In both cases, the mutation should primarily affect the electric field imparted on the carbonyl bond. A previous computational study has alluded to the fact that a water molecule could be present in the cavity between the Asp_{40}, steroid, and Tyr_{57}.[39] Addition of the water molecule there significantly reduced the pK_a of Asp_{40} by several units and produced reaction profiles similar to experimental values. It is possible that water from the bulk solution can have a significant effect on the reaction profile for these 3-chlorotyrosine mutants, specifically in the reprotonation step.

Evaluation of the Electric Field at the Geometric Center of a Bond

Previous studies have evaluated the electric field at two nuclei that make up a bond, and take an average of the bond projected field,[4,7,36] and other studies have evaluated the electric field at the geometric midpoint of the bond of interest.[21,35] We first evaluate the magnitude of the electric field, $|\mathbf{E}(\mathbf{r})|$, and the projection of $\mathbf{E}(\mathbf{r})$ along the corresponding bonds at the geometric center of the bonds. $\mathbf{E}(\mathbf{r})$ is calculated from $\rho(\mathbf{r})$, the nuclei, and the external field ($\mathbf{E}_{\text{ext}}(\mathbf{r})$):

$$\boldsymbol{E}(\boldsymbol{r}) = -\int d^3\boldsymbol{r}' \frac{\rho(\boldsymbol{r}')(\boldsymbol{r}' - \boldsymbol{r})}{|\boldsymbol{r}' - \boldsymbol{r}|} + \sum_i \frac{Z_i(\boldsymbol{R}_i - \boldsymbol{r})}{|\boldsymbol{R}_i - \boldsymbol{r}|} + \boldsymbol{E}_{ext}(\boldsymbol{r}) \quad (1)$$

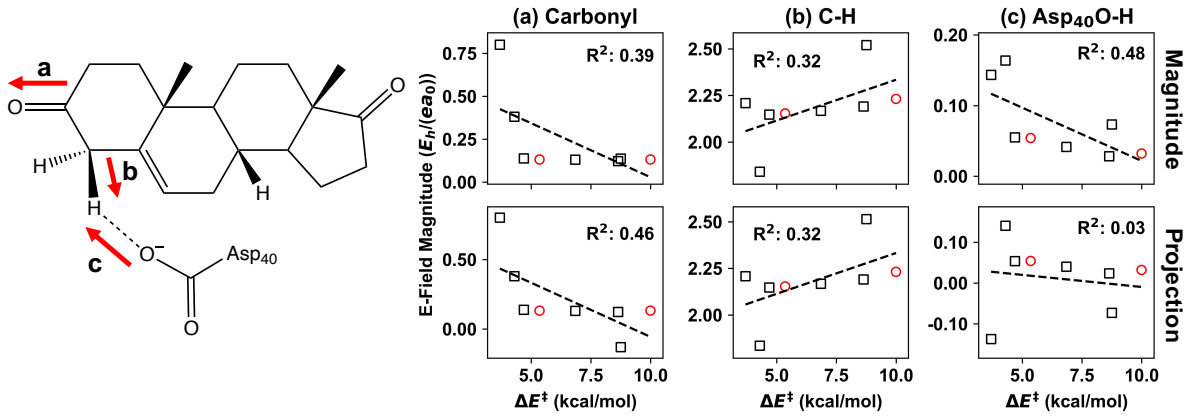

Figure 3: Electric field analysis at the geometric center of the bonds on the left. Carbonyl represents bond (a), C-H represents bond (b), and Asp_{40}O-H represents bond (c). Red arrows point in direction $\boldsymbol{E}(\boldsymbol{r})$ was projected onto. Red circles are KSI-Y^{32} and KSI-Y^{57} (included in linear regression). Top row is the magnitude of the electric field and bottom row is the magnitude of the projection along the bond. $\boldsymbol{E}(\boldsymbol{r})$ is in atomic units, $E_h/(ea_0)$. R^2 values are shown in each graph.

In general, we have found that there is a poor correspondence between both the electric field magnitude and projection along the bond line with the reaction barrier (Figure 3). Additionally, the directions of the best-fit lines do not correspond to physically expectant trends. These trends suggest that the higher the magnitude of the electric field that points towards the oxygen in the carbonyl (**a**), the lower the barrier (although the correlation is not great, see Figure 3**a**). Classically, the force on a charged particle is given as $\mathbf{F} = q\mathbf{E}(\mathbf{r})$, thus the force on an electron will be in the opposite direction of the electric field. The field pointing in this direction, at the carbonyl, should push electron density away from the oxygen, which should deactivate the carbonyl, thus, making the barrier higher. For the region of deprotonation, the trends indicate that the greater the electric field that points towards the hydrogen at the C-H bond (**b**), the higher the barrier. Again, chemically, we would expect that the electron density migrates from the hydrogen to the carbon as this bond breaks, and the bond between the Asp_{40}O and hydrogen forms. The electric field (**b**) should therefore facilitate this movement and promote the deprotonation step, contrary to the trend in Figure 3**b**. Field (**c**), despite having practically no correlation with the barrier, further contradicts physical intuition. The trend would suggest that if the field actually points towards Asp_{40}O, the barrier is higher (Figure 3**c**). But this field would push electron

density towards the hydrogen, and the substrate, which should actually lower the barrier. Overall, we see that calculating the electric field at the geometric center of the bond does not reliably produce the correct and expected physical trends. Instead, it can produce counter-intuitive relationship that ultimately lead to contradictions. Note, however, that these results do not disagree with those of Boxer.[24] The methods utilized by Boxer investigate how the electric field produced directly affect the carbonyl's bond stretching, which is a property that is integrated over the entire chemical bond rather than a single point. In fact, as will be shown later, our findings confirm the results of Boxer.

Evaluation of the Electric Field at the BCP from QTAIM

Arguably, a better location to evaluate the electric field than the geometric center of a bond could be proposed based on QTAIM. QTAIM is a mathematically rigorous formulation that partitions $\rho(\mathbf{r})$ into atomic basins that are separated by zero-flux surfaces.[40,41] That is, there exists surfaces between atomic basins such that given the normal vector to the surface, $\mathbf{n}(\mathbf{r})$, $\nabla\rho(\mathbf{r}) \cdot \mathbf{n}(\mathbf{r}) = \mathbf{0}$ everywhere along the surface. Additionally, critical points of $\rho(\mathbf{r})$ occur when $\nabla\rho(\mathbf{r}) = 0$. There are 4 types of critical points - nuclear, bond, ring, and cage - which are defined based upon the curvature of $\rho(\mathbf{r})$ at that point (Figure 4A). For example, nuclear critical points correspond to the location of atomic nuclei and are local maxima in all spatial directions of $\rho(\mathbf{r})$. Bond critical points (BCP) are saddle points that are minima in one direction, but maxima in all other spatial direction and lay on a maximal ridge between two nuclear critical points (Figure 4A). Mathematically, critical points are determined by first evaluating the hessian of ρ at $\mathbf{r_c}$, $\mathbf{J}(\nabla\rho)|_{\mathbf{r}=\mathbf{r_c}}$.

$$\mathbf{J}(\nabla\rho)|_{\mathbf{r}=\mathbf{r_c}} = \begin{bmatrix} \rho_{x,x} & \rho_{x,y} & \rho_{x,z} \\ \rho_{y,x} & \rho_{y,y} & \rho_{y,z} \\ \rho_{z,x} & \rho_{z,y} & \rho_{z,z} \end{bmatrix}\Bigg|_{\mathbf{r}=\mathbf{r_c}} \tag{2}$$

Let λ_1, λ_2, and λ_3 be the 3 eigenvalues of $\mathbf{J}(\nabla\rho)|_{\mathbf{r}=\mathbf{r_c}}$.. Taking the algebraic sum of the signs of λ_1, λ_2, and λ_3 to be ω, ω can either be 3, 1, -1, or -3. This corresponds to a nuclear point, BCP, ring critical point, or cage critical point respectively.

Since the electric field is related to force via $\mathbf{F} = q\mathbf{E}(\mathbf{r})$, it is initially thought that there would be a strong relationship between the electric field at BCPs and the reaction barrier. Since BCPs exist on the zero-flux surface that separates two atomic basins, $\mathbf{E}(\mathbf{r})$ at a BCP

should give a sense of the force acting on the electron density to move from one atomic basin to another.

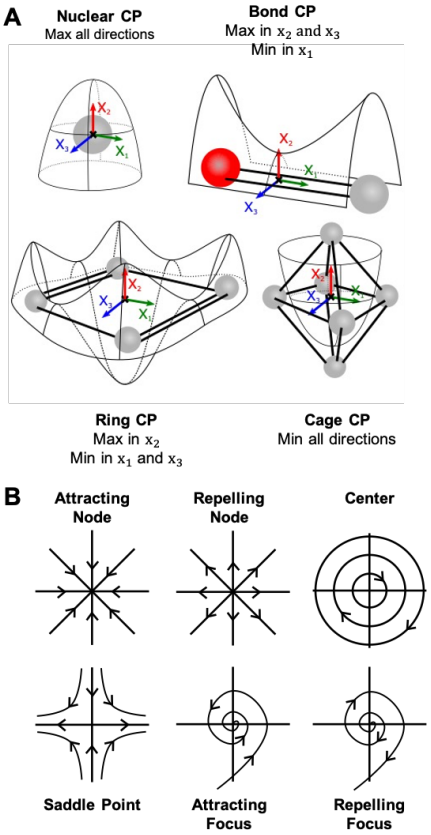

Figure 4: A) Schematic showing the various critical points within QTAIM. Isosurfaces of $\rho(\mathbf{r})$ are shown. The type of critical point depends on if $\rho(\mathbf{r})$ is a maximum or minimum for the $x_1, x_2,$ and x_3 directions. This can be determined by the algebraic sum of the sign of the eigenvalues of the hessian of $\rho(\mathbf{r})$ at the critical point. B) Various topological features present within a 2D vector field. Points are identified mathematically by considering the real and imaginary eigenvectors of the differential of the vector field at each critical point.

As such, $\mathbf{E}(\mathbf{r})$ was calculated at the carbonyl BCP as well as along the Asp_{40}O-H-C BCPs that participate in the deprotonation of the substrate (Figure 5). If we were only to consider the wild-type KSI structures (WT, *r*+, *r*−, *g*+, *b*+, *b*−), then $|\mathbf{E}(\mathbf{r})|$ and the projection of $\mathbf{E}(\mathbf{r})$ along each bond yields a fairly linear relationship for each BCP (Figure 5). Additionally, these relationships should be chemically expected. Projection of $\mathbf{E}(\mathbf{r})$ at the Asp_{40}O-H BCP illustrates that a weaker barrier arises when the field points towards the oxygen, and away from the hydrogen (Figure 5**b**). This corresponds to a stronger force that moves electrons towards the hydrogen. Similarly, projection of $\mathbf{E}(\mathbf{r})$ at the C-H BCP shows

that a smaller barrier arises when the **E**(**r**) points more towards the hydrogen (Figure 5**c**). This produces a stronger force that will move electron density to the carbon. Thus, a lower barrier is calculated when the electric field aligns in such a way as to create a force that moves electrons from $Asp_{40}O$ towards the substrate, as would be expected. For the carbonyl, the electric field that is less aligned with the bond, and the less it points towards the oxygen, the smaller the barrier (Figure 5**a**). The optimal field produces a smaller force that moves electron density to the carbon, and therefore, the carbonyl is more activated, facilitating the first step in the reaction. That is, more negative charge can accumulate on the carbonyl oxygen. These relationships agree with chemical expectations and previous studies.[17,24]

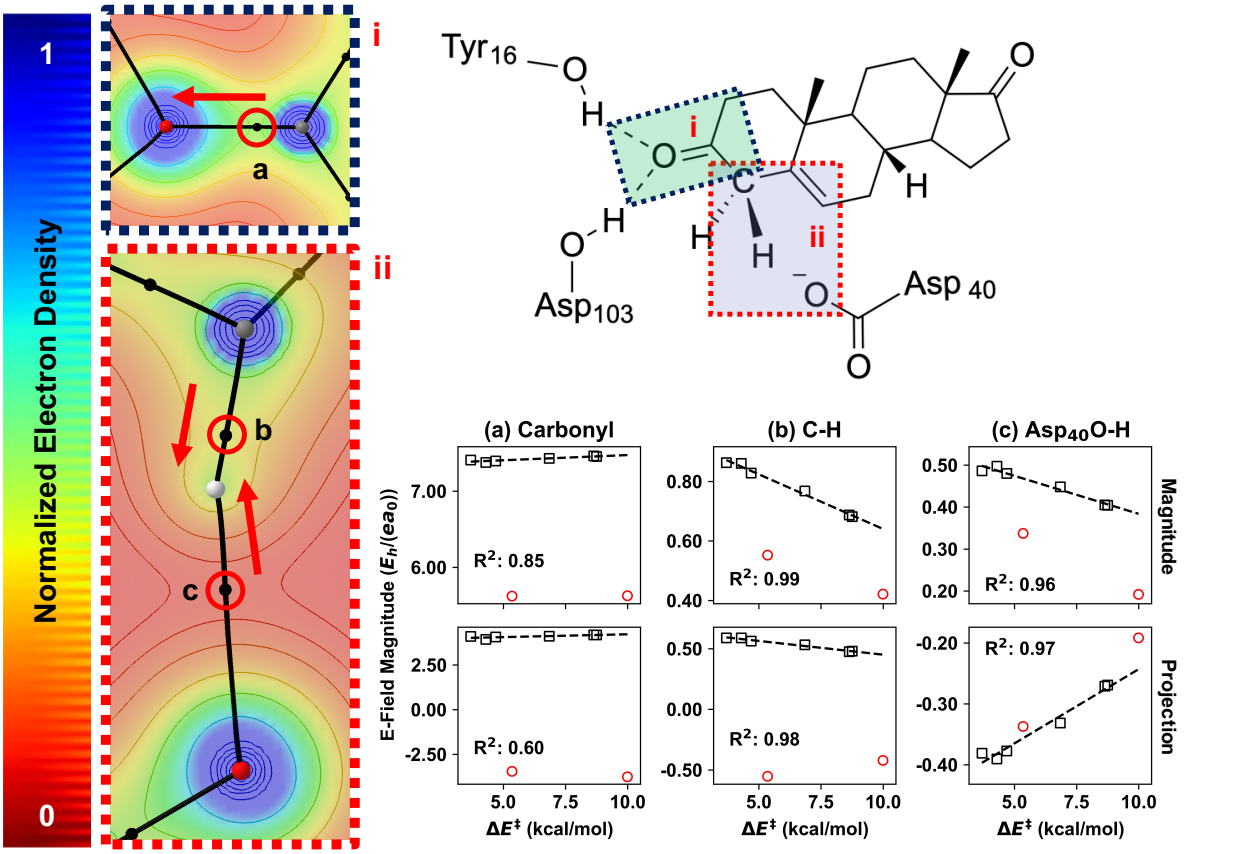

Figure 5: Location of BCPs where the electric field was computed. Top right illustrates location of $\rho(\mathbf{r})$ graphs on the left. i and ii illustrate the spatial distribution of $\rho(\mathbf{r})$ as well as the location of BCP (a-c). Red arrows show direction of the bond the electric field was projected onto. Graphs show **E**(**r**) (in atomic units, $E_h/(ea_0)$ versus $\Delta E^{\ddagger}$ at BCPs a-c. Red circles are KSI-Y[32] and KSI-Y[57] (excluded from linear regression). Top row is the magnitude of the electric field and bottom row is the magnitude of the projection along the bond as shown in i and ii. R^2 values are shown in each graph. Note that in column (**a**), their appears to be a strong correlation; however, proper rescaling of the y-axis will illustrate that the correlation is not that strong and is in agreement with the R^2 values (Figure S1).

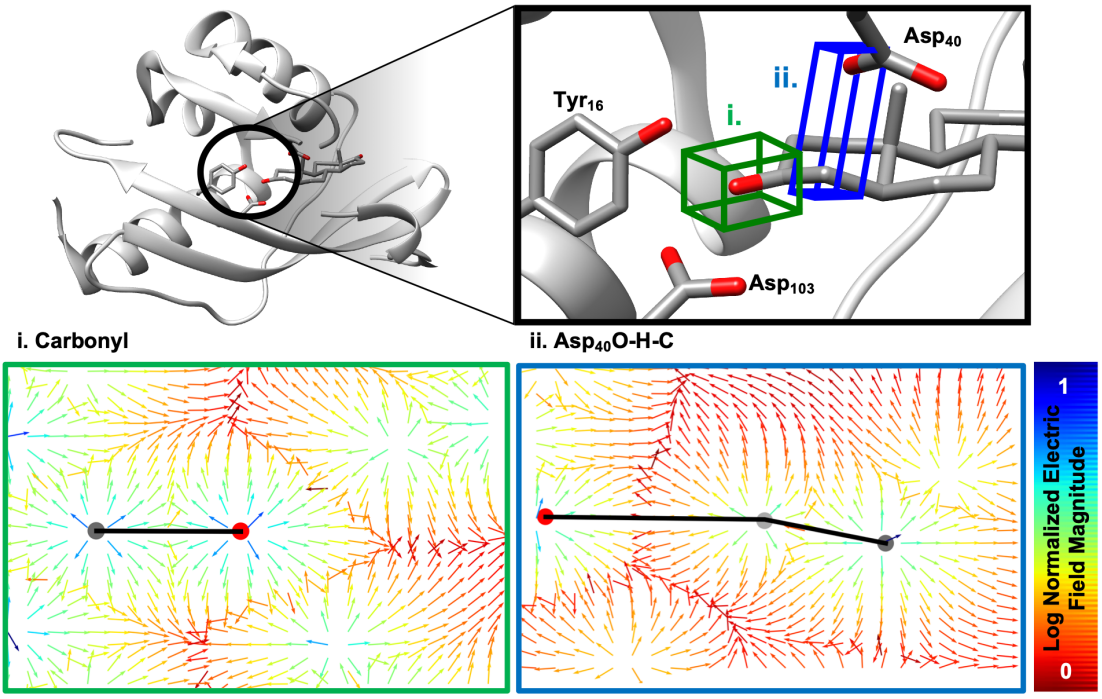

Figure 6: Regions within KSI that were analyzed via the global distribution of streamlines. i and ii refer to regions in Figure 5. Within the vector fields, the oxygen (red), hydrogen (light gray), and carbon (gray), along with the bonds connecting the atoms, are shown. Note topological features include repelling nodes, attracting nodes, and saddle points.

However, KSI-Y^{32} and KSI-Y^{57} do not follow the trend and become outliers in almost all of the plots (red circles in Figure 5 plots). In fact, we see a reversal of the effect of the electric field projection at the carbonyl, which would lead to a naive suggestion that these mutants significantly change the electric field at this bond to something different in comparison to the other structures (Figure 5). As such, even using a more physically motivated point is not robust enough to analyze the electric field across various perturbations of the local electric field in KSI.

If deciding to use singular points to characterize $\mathbf{E}(\mathbf{r})$, it has to be assumed that $\mathbf{E}(\mathbf{r})$ is at least Lipschitz continuous around the points of interest with a fairly small Lipschitz constant. That is, if we are interested in $\mathbf{E}(\mathbf{r})$ at some point $\mathbf{r}^*$, then for some neighborhood U of $\mathbf{r}^*$, there is a positive constant K such that for all $\mathbf{r}_i$ and $\mathbf{r}_j$ in U,

$$\left|\boldsymbol{E}(\boldsymbol{r}_i) - \boldsymbol{E}(\boldsymbol{r}_j)\right| \leq K\left|\boldsymbol{r}_i - \boldsymbol{r}_j\right| \tag{3}$$

The minimal constant K such that Equation 3 still holds is said to be the best Lipschitz constant. If $\mathbf{E}(\mathbf{r})$ is not Lipschitz continuous or K is very large, small deviations in the choice of the point can cause very large differences in the calculated $\mathbf{E}(\mathbf{r})$. When we are analyzing single points, we are disregarding the various topological features present within the vector field (Figure 4B). For a 2D vector field, there are a total of 6 different topological features that arise from critical points (when $\mathbf{E}(\mathbf{r}) = 0$). These features are determined by the eigenvalues of the differential of the vector field evaluated at the critical point (Equation 4).

$$d\mathbf{E}|_{\mathbf{r}=\mathbf{r_c}} = \begin{bmatrix} \frac{\partial \mathbf{E}_x}{\partial x} & \frac{\partial \mathbf{E}_x}{\partial y} & \frac{\partial \mathbf{E}_x}{\partial z} \\ \frac{\partial \mathbf{E}_y}{\partial x} & \frac{\partial \mathbf{E}_y}{\partial y} & \frac{\partial \mathbf{E}_y}{\partial z} \\ \frac{\partial \mathbf{E}_z}{\partial x} & \frac{\partial \mathbf{E}_z}{\partial y} & \frac{\partial \mathbf{E}_z}{\partial z} \end{bmatrix}_{\mathbf{r}=\mathbf{r_c}} = -\begin{bmatrix} \Phi_{x,x} & \Phi_{x,y} & \Phi_{x,z} \\ \Phi_{y,x} & \Phi_{y,y} & \Phi_{y,z} \\ \Phi_{z,x} & \Phi_{z,y} & \Phi_{z,z} \end{bmatrix}_{\mathbf{r}=\mathbf{r_c}} \quad (4)$$

However, because $\mathbf{E}(\mathbf{r}) = -\nabla\Phi(\mathbf{r})$, $d\mathbf{E}$ will only have real eigenvalues meaning that the electric field will not have a center, attracting focus, or repelling focus (Figure 4B). This is equivalent to noticing that the curl, $\nabla \times \mathbf{E}(\mathbf{r})$, is zero everywhere, thus the electric field does not have any regions that are spinning. Furthermore, analyzing single points is not invariant under rotational or translational transformations. Indeed, it can be seen from a plot of the electric field that vector field is very sensitive to the position, and is in no way homogenous; hence, choosing a single point can be devastating for trying to capture how the electric field is actually changing (Figure 6). Additionally, in the 2D plots in Figure 6, one can see topological features that include attracting nodes, repelling nodes, and saddle points. Analyzing the electric field by only considering specific points is still, to some extent, arbitrary. Calculating $\mathbf{E}(\mathbf{r})$ at a specific point is a local quantity of the electric field and does not capture the geometrical nature of the image of $\mathbf{E}(\mathbf{r})$.

Global Distribution of Streamlines to Evaluate Changes in the Electric Field Topology

In order to analyze larger regions of $\mathbf{E}(\mathbf{r})$ and detect how changes in the geometry of the vector field correlate with the reaction barrier, a new approach is warranted. Analysis of vector fields is largely popular in the field of fluid dynamic,[42–46] where a method of determining the similarity between vector fields has been constructed by using global

distributions arising from the streamlines.[47] This method has been shown to be invariant under rotational and translation, and partially invariant under scaling of vector fields. In this study, we apply this algorithm to analyze local changes in $\mathbf{E}(\mathbf{r})$.

We begin by defining boxes that enclose chemically relevant subsets of $\mathbf{E}(\mathbf{r})$: a $4 \times 4 \times 2$ Å box around the carbonyl and the Asp_{40}O-H-C bonds (Figure 6), regions i and ii in Figure 5. In these regions, the electric field can point in any direction and the magnitude can range from 0.001 a.u. to 38300 a.u. (Figure 6). The very large electric field magnitudes are located around the nuclei. We then randomly sample two points that lie on the same streamline, α, and bin them by Euclidean distance and mean curvature. We compute the curvature at each point using Equation 5.

$$\kappa = \frac{|\alpha' \times \alpha''|}{|\alpha'|^3} = \frac{|\boldsymbol{E}(\boldsymbol{r}) \times \boldsymbol{E}'(\boldsymbol{r})|}{|\boldsymbol{E}(\boldsymbol{r})|^3} \tag{5}$$

For each region, we construct a 2D histogram (200×200 in size) of Euclidean distance versus curvature using 100,000 randomly sampled pairs of points (See Supp Info). Then we define the χ^2 distance between two, N-bin normalized histograms f and g as:

$$\chi^2 : D(f, g) = \frac{1}{2} \sum_{i=1}^{N} \frac{(f[i] - g[i])^2}{f[i] + g[i]} \tag{6}$$

The range of χ^2 is [0,1] with 0 representing the same histogram and 1 representing completely different histograms.

Using this method, we can construct a distance matrix for the carbonyl region (Figure 7). Each square pictorially represents the distance between their corresponding 2D histograms, with 0 (black) being the same histogram, and 1 (white) being completely different. The diagonal will always be black as this corresponds to the same histogram. We can therefore see that *g*+, *b*+, and *r*+ all have very similar electric fields in the carbonyl region. These three structures are slightly similar to NEF (wild-type KSI with no external field) and KSI-Y^{32}, and very different from *b*−, *r*−, and KSI-Y^{57}. Similarly, we can see that *b*− and *r*− are very similar to each other, and slightly similar to NEF and KSI-Y^{32}. Recall that *g*+, *b*+, and *r*+ all decreased the first reaction barrier, and *b*−, *r*− increased the barrier (Figure 2). KSI-Y^{57} increased the barrier much more than both *b*−, *r*− (Figure 2). Our method has clustered the structures in agreement with how they affected the barrier. Analysis of the region undergoing

deprotonation (ii in Figure 5) shows that *b*+ and *r*+ are very similar, *g*+ and NEF are very similar, and *b*− and *r*− are very similar (Figure 7). Again, these are more or less grouped by how they affect the first barrier. Though, in the region undergoing deprotonation, we do see that *b*+ and *r*+ are more similar to *b*− and *r*− as compared to the carbonyl region. Additionally, KSI-Y^{57} is similar to almost all of the structures, despite having the most different barrier. The plotted fields for all considered systems are provided in the SI.

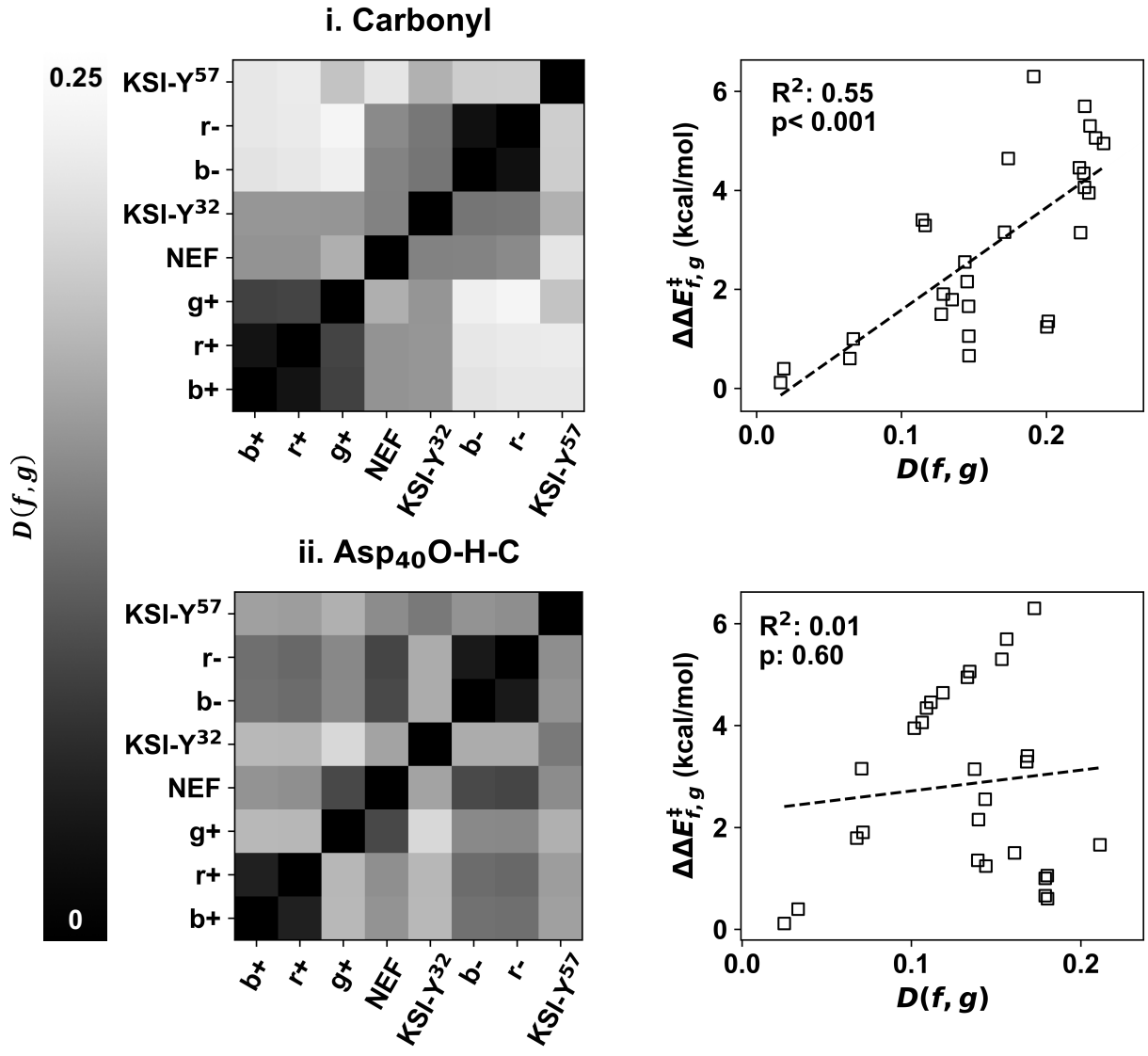

Figure 7: Dissimilarity measurement between systems with different applied external electric fields. i. represents analysis of the region around the carbonyl and ii. the region around the Asp_{40}O-H-C region (regions contextualized within Figure 5 and Figure 6). In the dissimilarity matrices on the left, black means the same and white means different. Graphs on the right compare the change in the reaction barrier between two system ($\Delta\Delta E^{\ddagger}_{f,g}$) to the distance between their histograms ($D(f,g)$) or

the value within the matrix on the left. R^2 and p-value are shown with each graph. NEF: wild-type KSI with no external field.

Having calculated the dissimilarity, or distance, between each pair of systems with varying external electric fields, we compare the difference in reaction barriers for each pair. We would expect that for the more similar the barrier ($\Delta\Delta E^{\ddagger}_{f,g}$ close to 0), the difference between the two electric fields should be minimal ($D(f,g)$ close to 0). Similarly, for large $\Delta\Delta E^{\ddagger}_{f,g}$, we would expect to see a larger distance between histograms ($D(f,g)$ closer to 1). $\Delta\Delta E^{\ddagger}_{f,g}$ was plotted versus $D(f,g)$ for both regions (Figure 7). The local electric field around the carbonyl has a strong relationship with the reaction barrier ($R^2 = 0.55$), whereas the local electric field around the site of deprotonation ($R^2 = 0$) did not (Figure 7). Hence, electric fields that are similar around the carbonyl bond correspond to similar barriers. Though, it is expected to not necessarily see a correlation at the site of deprotonation as both the external electric fields and mutations directly impact that carbonyl bond and should not impact the region of deprotonation directly. Hence, we would not expect to see changes in the electric field topology around the deprotonation site as a function of the reaction barrier. Though at the same time, we would not expect the electric field to be the same across all of these structures as there are differences in the electron density and nuclear coordinates. In general, around the carbonyl, the more similar the electric field topology is, as measured by the global distribution, the more similar the barriers for deprotonation are. And the more dissimilar the electric fields are, the further apart the barriers are.

We further evaluate our method sensitivity to the reactant state destabilization, and the TS stabilization, by decomposing $\Delta E^{\ddagger}$ into the relative change in energy for the reactant state and first TS (deprotonation). Recently, Boxer has shown that KSI's electrostatic preorganization operates by stabilizing the transition state, and only minimally destabilizes the ground state. Further, from the plot shown it becomes clear that the electric field does not always shift both the TS and reactant in the same direction. In fact, for the electric field applied along the carbonyl bond (r), we see that r+ destabilizes the reactant and stabilizes the TS (Figure 8). r− on the other hand, greatly stabilizes the reactant state, and only slightly stabilizes the TS. However, when we apply the external field from the carbonyl oxygen to the α-carbon (b), we see that b+ destabilizes the reactant and TS but destabilizes the

reactant more so. Additionally, $b-$ stabilizes both reactant and TS, but expectantly stabilizes the reactant more so. When we then compare $\Delta E_{reactant}$ versus $D(f,g)$, given from the electric field histograms, we actually see a decrease in the correlation (Supp Info). This indicates that the electric field we are analyzing is not just indicative of relative shifts in the ground state, but also in relative shifts of the transition state fully allowing us to probe the electrostatic preorganization.

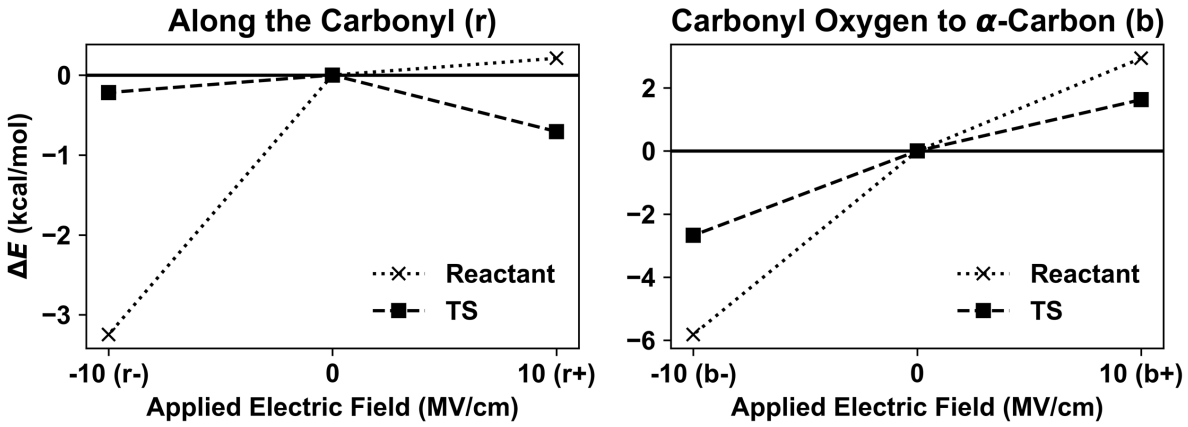

Figure 8: Contribution of the external electric field perturbation to shift in the reaction barrier. Positive values of ΔE indicate destabilization and negative values indicate stabilization relative to KSI-WT. r and b correspond to directions defined in Figure 1.

Conclusions

A protein's electric field has been fairly elusive, as many studies have used either indirect, or incomplete methods to analyze and quantify this field. A robust method of quick and rigorous analysis of the field, which predicts changes in the barrier of the catalyzed reaction due to changes in the field in protein variants, without needing to compute a TS, will greatly facilitate computation efforts to understand the functionality of natural enzymes, and design artificial enzymes of high activity. Very few studies look directly at the electric field and those that do only consider specific points of the electric field,[7,24,36] neglecting the global geometry of the field.

In this study, we have shown how traditional methods of analyzing the electric vector field by considering only specific points neglects the broader topology of the electric vector field and can lead to incorrect and unphysical conclusions. When we consider the electric field at the geometric center of the bonds of interest, we see unphysical trends in relation to

the reaction barrier (Figure 3). Using a more physically motivated location, the BCP from QTAIM, we saw better correlations for the systems where we apply an external electric field; however, we the 3-chlorotyrosine mutants remained outliers (Figure 5). Thus, it is possible to evaluate the electric field at BCPs, though the perturbation to the system must be small, and may not be able to accurately quantify the variation introduced by residue mutations. Instead, consideration of the vector field topology enables us to more accurately compare the differences between locally produced, or more generally produced, molecular electric fields. The ability to quantify differences in the electric field will allow us to calculate relative electrostatic preorganization for a protein and its mutants. Previous studies have shown that KSI creates an optimal electric field so as to activate the carbonyl in the reactant state.[15,17,24] While KSI features a chemically simplistic protonation/deprotonation reaction, our method of considering the global distribution of streamlines has allowed us to quantitatively assess the perturbations in the locally produced electric field and correlated these changes to the reaction barrier. Additionally, we were able to use our method across both artificially applied electric fields, and actual amino acid mutations that have been shown to cause changes in the reaction rate. Our findings further bolster that an optimal electric field that activates the substrates carbonyl can greatly improve the reaction rate of KSI.

The proposed method will enable researches to better analyze protein electric fields and how they change either through mutations, or dynamically within the native dynamics of the protein. Our study compliments the linear Stark spectroscopy work done by Boxer showing that the KSI protein exerts an electric field on the order of 100 MV/cm on the substrate carbonyl[24], and all of the subsequent studies illustrating the importance of the field around the carbonyl.[4,26,39] Thus, our method can complement experimental works which are unable to directly look at the electric field and complement studies which use linear Stark spectroscopy to investigate changes in the electric field. The method we have shown only relies on the ground state wavefunction, which is easily computed in comparison to finding the reaction barrier. This method of analysis could also be used to evaluate the electric field as calculated from force field charges of the whole protein, to understand and predict how distant mutations affect the electric field within this active site.

It is important to note that this method still requires chemical and physical intuition to study the proper bond region that would be most greatly influenced by an electric field.

Methods

Geometry optimization calculations with the M06-2X functional[48] and single valence with polarization (def2-SVP) basis set were performed in Turbomole (V6.3).[49,50,59,51–58] Numerical frequency calculations were performed to ensure structures were at a minimum. The triple-ζ with polarization (def2-TZVP) basis set was used for single point calculations. Implicit solvation was modeled using the conductor-like screening model (COSMO)[60] with the dielectric constant set to 4, which is typical for buried active sites.[61] All calculations were consistent with our previous study.[16] The nature of stationary points was confirmed by frequency calculations: 0 imaginary frequencies for reaction intermediates and 1 imaginary frequency for TS. QTAIM analysis was performed using the AIMALL software[62] to locate BCP.[41,63,64]

A grid was applied to discretize the electric vector field and at each grid point $\mathbf{E}(\mathbf{r})$ was calculated from the wavefunction in Turbomole. Turbomole uses Equation 1 to calculate the electric field from the electron density and nuclear coordinates. A grid of $100 \times 100 \times 50$, or 500,000 points, was used for each region analyzed. Further optimization of the region analyzed around the carbonyl should increase the correlation between the field similarity and the barrier. The regions analyzed can include other nuclei that can enter and leave the region causing changes in the similarity measurements, when the field in the region of interest is not changing very much.

Supporting Information Available

Plotted fields, 2D histograms of curvature versus Euclidean distance, $\Delta E_{reactant}$ versus $D(f, g)$, dependence on functional and basis set, and structure coordinates for KSI-Y[32] and KSI-Y[57]. This information is available free of charge on the ACS Publications website.

Acknowledgement

This work was supported by the National Science Foundation grant CHE-1903808 and used the Extreme Science and Engineering Discovery Environment (XSEDE) Bridges system at

the Pittsburgh Supercomputing Center (PSC). We also acknowledge the UCLA-IDRE cluster Hoffman2 computational resources.

References

(1) Warshel, A. Electrostatic Origin of the Catalytic Power of Enzymes and the Role of Preorganized Active Sites. *J. Biol. Chem.* **1998**, *273* (42), 27035–27038. https://doi.org/10.1074/jbc.273.42.27035.

(2) Fried, S. D.; Boxer, S. G. Electric Fields and Enzyme Catalysis. *Annu. Rev. Biochem.* **2017**, *86* (1), 387–415. https://doi.org/10.1146/annurev-biochem-061516-044432.

(3) Warshel, A.; Sharma, P. K.; Kato, M.; Xiang, Y.; Liu, H.; Olsson, M. H. M. M. Electrostatic Basis for Enzyme Catalysis. *Chem. Rev.* **2006**, *106* (8), 3210–3235. https://doi.org/10.1021/cr0503106.

(4) Wang, L.; Fried, S. D.; Markland, T. E. Proton Network Flexibility Enables Robustness and Large Electric Fields in the Ketosteroid Isomerase Active Site. *J. Phys. Chem. B* **2017**, *121* (42), 9807–9815. https://doi.org/10.1021/acs.jpcb.7b06985.

(5) Morgenstern, A.; Jaszai, M.; Eberhart, M. E.; Alexandrova, A. N. Quantified Electrostatic Preorganization in Enzymes Using the Geometry of the Electron Charge Density. *Chem. Sci.* **2017**, *8* (7), 5010–5018. https://doi.org/10.1039/c7sc01301a.

(6) Visser, S. P. Second-Coordination Sphere Effects on Selectivity and Specificity of Heme and Nonheme Iron Enzymes. *Chem. – A Eur. J.* **2020**, *26* (24), 5308–5327. https://doi.org/10.1002/chem.201905119.

(7) Welborn, V. V.; Head-Gordon, T. Fluctuations of Electric Fields in the Active Site of the Enzyme Ketosteroid Isomerase. *J. Am. Chem. Soc.* **2019**, *141* (32), 12487–12492. https://doi.org/10.1021/jacs.9b05323.

(8) Röthlisberger, D.; Khersonsky, O.; Wollacott, A. M.; Jiang, L.; DeChancie, J.; Betker, J.; Gallaher, J. L.; Althoff, E. A.; Zanghellini, A.; Dym, O.; Albeck, S.; Houk, K. N.; Tawfik, D. S.; Baker, D. Kemp Elimination Catalysts by Computational Enzyme Design. *Nature* **2008**, *453* (7192), 190–195. https://doi.org/10.1038/nature06879.

(9) Privett, H. K.; Kiss, G.; Lee, T. M.; Blomberg, R.; Chica, R. A.; Thomas, L. M.; Hilvert, D.; Houk, K. N.; Mayo, S. L. Iterative Approach to Computational Enzyme Design. *Proc. Natl. Acad. Sci.* **2012**, *109* (10), 3790–3795.

https://doi.org/10.1073/pnas.1118082108.

(10) Siegel, J. B.; Zanghellini, A.; Lovick, H. M.; Kiss, G.; Lambert, A. R.; St.Clair, J. L.; Gallaher, J. L.; Hilvert, D.; Gelb, M. H.; Stoddard, B. L.; Houk, K. N.; Michael, F. E.; Baker, D. Computational Design of an Enzyme Catalyst for a Stereoselective Bimolecular Diels-Alder Reaction. *Science (80-.).* **2010**, *329* (5989), 309–313. https://doi.org/10.1126/science.1190239.

(11) Rajagopalan, S.; Wang, C.; Yu, K.; Kuzin, A. P.; Richter, F.; Lew, S.; Miklos, A. E.; Matthews, M. L.; Seetharaman, J.; Su, M.; Hunt, J. F.; Cravatt, B. F.; Baker, D. Design of Activated Serine–Containing Catalytic Triads with Atomic-Level Accuracy. *Nat. Chem. Biol.* **2014**, *10* (5), 386–391. https://doi.org/10.1038/nchembio.1498.

(12) Jiang, L.; Althoff, E. A.; Clemente, F. R.; Doyle, L.; Rothlisberger, D.; Zanghellini, A.; Gallaher, J. L.; Betker, J. L.; Tanaka, F.; Barbas, C. F.; Hilvert, D.; Houk, K. N.; Stoddard, B. L.; Baker, D. De Novo Computational Design of Retro-Aldol Enzymes. *Science (80-.).* **2008**, *319* (5868), 1387–1391. https://doi.org/10.1126/science.1152692.

(13) Pollack, R. M. Enzymatic Mechanisms for Catalysis of Enolization: Ketosteroid Isomerase. *Bioorg. Chem.* **2004**, *32* (5), 341–353. https://doi.org/10.1016/j.bioorg.2004.06.005.

(14) Hawkinson, D. C.; Eames, T. C. M.; Pollack, R. M. Energetics of 3-Oxo-.DELTA.5-Steroid Isomerase: Source of the Catalytic Power of the Enzyme. *Biochemistry* **1991**, *30* (45), 10849–10858. https://doi.org/10.1021/bi00109a007.

(15) Warshel, A.; Sharma, P. K.; Chu, Z. T.; Åqvist, J. Electrostatic Contributions to Binding of Transition State Analogues Can Be Very Different from the Corresponding Contributions to Catalysis: Phenolates Binding to the Oxyanion Hole of Ketosteroid Isomerase †. *Biochemistry* **2007**, *46* (6), 1466–1476. https://doi.org/10.1021/bi061752u.

(16) Fuller III, J.; Wilson, T. R.; Eberhart, M. E.; Alexandrova, A. N.; Fuller, J.; Wilson, T. R.; Eberhart, M. E.; Alexandrova, A. N. Charge Density in Enzyme Active Site as a Descriptor of Electrostatic Preorganization. *J. Chem. Inf. Model.* **2019**, *59* (5), 2367–2373. https://doi.org/10.1021/acs.jcim.8b00958.

(17) Layfield, J. P.; Hammes-Schiffer, S. Calculation of Vibrational Shifts of Nitrile Probes in the Active Site of Ketosteroid Isomerase upon Ligand Binding. *J. Am. Chem. Soc.* **2013**,

135 (2), 717–725. https://doi.org/10.1021/ja3084384.

(18) Kamerlin, S. C. L.; Sharma, P. K.; Chu, Z. T.; Warshel, A. Ketosteroid Isomerase Provides Further Support for the Idea That Enzymes Work by Electrostatic Preorganization. *Proc. Natl. Acad. Sci.* **2010**, *107* (9), 4075–4080. https://doi.org/10.1073/pnas.0914579107.

(19) Park, H.; Merz, K. M. Molecular Dynamics and Quantum Chemical Studies on the Catalytic Mechanism of Δ 5 -3-Ketosteroid Isomerase: The Catalytic Diad versus the Cooperative Hydrogen Bond Mechanism. *J. Am. Chem. Soc.* **2003**, *125* (4), 901–911. https://doi.org/10.1021/ja0208097.

(20) Houck, W. J.; Pollack, R. M. Temperature Effects on the Catalytic Activity of the D38E Mutant of 3-Oxo-Δ 5 -Steroid Isomerase: Favorable Enthalpies and Entropies of Activation Relative to the Nonenzymatic Reaction Catalyzed by Acetate Ion. *J. Am. Chem. Soc.* **2004**, *126* (50), 16416–16425. https://doi.org/10.1021/ja046819k.

(21) Kędzierski, P.; Zaczkowska, M.; Sokalski, W. A. Extreme Catalytic Power of Ketosteroid Isomerase Related to the Reversal of Proton Dislocations in Hydrogen-Bond Network. *J. Phys. Chem. B* **2020**, *124* (18), 3661–3666. https://doi.org/10.1021/acs.jpcb.0c01489.

(22) Kraut, D. A.; Sigala, P. A.; Pybus, B.; Liu, C. W.; Ringe, D.; Petsko, G. A.; Herschlag, D. Testing Electrostatic Complementarity in Enzyme Catalysis: Hydrogen Bonding in the Ketosteroid Isomerase Oxyanion Hole. *PLoS Biol.* **2006**, *4* (4), e99. https://doi.org/10.1371/journal.pbio.0040099.

(23) Herschlag, D.; Natarajan, A. Fundamental Challenges in Mechanistic Enzymology: Progress toward Understanding the Rate Enhancements of Enzymes. *Biochemistry* **2013**, *52* (12), 2050–2067. https://doi.org/10.1021/bi4000113.

(24) Fried, S. D.; Bagchi, S.; Boxer, S. G. Extreme Electric Fields Power Catalysis in the Active Site of Ketosteroid Isomerase. *Science (80-.).* **2014**, *346* (6216), 1510–1514. https://doi.org/10.1126/science.1259802.

(25) Wu, Y.; Boxer, S. G. A Critical Test of the Electrostatic Contribution to Catalysis with Noncanonical Amino Acids in Ketosteroid Isomerase. *J. Am. Chem. Soc.* **2016**, *138* (36), 11890–11895. https://doi.org/10.1021/jacs.6b06843.

(26) Wu, Y.; Fried, S. D.; Boxer, S. G. A Preorganized Electric Field Leads to Minimal

Geometrical Reorientation in the Catalytic Reaction of Ketosteroid Isomerase. *J. Am. Chem. Soc.* **2020**, *142* (22), 9993–9998. https://doi.org/10.1021/jacs.0c00383.

(27) Vath, G. M.; Earhart, C. A.; Rago, J. V; Kim, M. H.; Bohach, G. A.; Schlievert, P. M.; Ohlendorf, D. H. The Structure of the Superantigen Exfoliative Toxin A Suggests a Novel Regulation as a Serine Protease † , ‡. *Biochemistry* **1997**, *36* (7), 1559–1566. https://doi.org/10.1021/bi962614f.

(28) Lameira, J.; Bora, R. P.; Chu, Z. T.; Warshel, A. Methyltransferases Do Not Work by Compression, Cratic, or Desolvation Effects, but by Electrostatic Preorganization. *Proteins Struct. Funct. Bioinforma.* **2015**, *83* (2), 318–330. https://doi.org/10.1002/prot.24717.

(29) Wang, Z.; Danovich, D.; Ramanan, R.; Shaik, S. Oriented-External Electric Fields Create Absolute Enantioselectivity in Diels–Alder Reactions: Importance of the Molecular Dipole Moment. *J. Am. Chem. Soc.* **2018**, *140* (41), 13350–13359. https://doi.org/10.1021/jacs.8b08233.

(30) Meir, R.; Chen, H.; Lai, W.; Shaik, S. Oriented Electric Fields Accelerate Diels-Alder Reactions and Control the Endo/Exo Selectivity. *ChemPhysChem* **2010**, *11* (1), 301–310. https://doi.org/10.1002/cphc.200900848.

(31) Shaik, S.; Mandal, D.; Ramanan, R. Oriented Electric Fields as Future Smart Reagents in Chemistry. *Nat. Chem.* **2016**, *8* (12), 1091–1098. https://doi.org/10.1038/nchem.2651.

(32) Arabi, A. A.; Matta, C. F. Effects of External Electric Fields on Double Proton Transfer Kinetics in the Formic Acid Dimer. *Phys. Chem. Chem. Phys.* **2011**, *13* (30), 13738. https://doi.org/10.1039/c1cp20175a.

(33) Arabi, A. A.; Matta, C. F. Effects of Intense Electric Fields on the Double Proton Transfer in the Watson–Crick Guanine–Cytosine Base Pair. *J. Phys. Chem. B* **2018**, *122* (37), 8631–8641. https://doi.org/10.1021/acs.jpcb.8b05053.

(34) Sowlati-Hashjin, S.; Matta, C. F. The Chemical Bond in External Electric Fields: Energies, Geometries, and Vibrational Stark Shifts of Diatomic Molecules. *J. Chem. Phys.* **2013**, *139* (14), 144101. https://doi.org/10.1063/1.4820487.

(35) Wang, X.; He, X.; Zhang, J. Z. H. Predicting Mutation-Induced Stark Shifts in the Active Site of a Protein with a Polarized Force Field. *J. Phys. Chem. A* **2013**, *117* (29), 6015–

6023. https://doi.org/10.1021/jp312063h.

(36) Zoi, I.; Antoniou, D.; Schwartz, S. D. Electric Fields and Fast Protein Dynamics in Enzymes. *J. Phys. Chem. Lett.* **2017**, *8* (24), 6165–6170. https://doi.org/https://doi.org/10.1021/acs.jpclett.7b02989.

(37) Raček, T.; Schindler, O.; Toušek, D.; Horský, V.; Berka, K.; Koča, J.; Svobodová, R. Atomic Charge Calculator II: Web-Based Tool for the Calculation of Partial Atomic Charges. *Nucleic Acids Res.* **2020**, *48* (W1), W591–W596. https://doi.org/10.1093/nar/gkaa367.

(38) Wu, Y.; Fried, S. D.; Boxer, S. G. Dissecting Proton Delocalization in an Enzyme's Hydrogen Bond Network with Unnatural Amino Acids. *Biochemistry* **2015**, *54* (48), 7110–7119. https://doi.org/10.1021/acs.biochem.5b00958.

(39) Feierberg, I.; Åqvist, J. The Catalytic Power of Ketosteroid Isomerase Investigated by Computer Simulation †. *Biochemistry* **2002**, *41* (52), 15728–15735. https://doi.org/10.1021/bi026873i.

(40) Bader, R. F. W. Atoms in Molecules. *Acc. Chem. Res.* **1985**, *18* (1), 9–15. https://doi.org/10.1021/ar00109a003.

(41) Bader, R. F. W. *The Quantum Theory of Atoms in Molecules*; Matta, C. F., Boyd, R. J., Eds.; Wiley, 2007. https://doi.org/10.1002/9783527610709.

(42) Chiao-Fe Shu; Jain, R. C. Vector Field Analysis for Oriented Patterns. *IEEE Trans. Pattern Anal. Mach. Intell.* **1994**, *16* (9), 946–950. https://doi.org/10.1109/34.310692.

(43) Helman, J. L.; Hesselink, L. Visualizing Vector Field Topology in Fluid Flows. *IEEE Comput. Graph. Appl.* **1991**, *11* (3), 36–46. https://doi.org/10.1109/38.79452.

(44) Helman, J.; Hesselink, L. Representation and Display of Vector Field Topology in Fluid Flow Data Sets. *Computer (Long. Beach. Calif).* **1989**, *22* (8), 27–36. https://doi.org/10.1109/2.35197.

(45) Tong, Y.; Lombeyda, S.; Hirani, A. N.; Desbrun, M. Discrete Multiscale Vector Field Decomposition. *ACM Trans. Graph.* **2003**, *22* (3), 445. https://doi.org/10.1145/882262.882290.

(46) Philippou, P. A.; Strickland, R. N. Vector Field Analysis and Synthesis Using Three-Dimensional Phase Portraits. *Graph. Model. Image Process.* **1997**, *59* (6), 446–462.

https://doi.org/10.1006/gmip.1997.0445.

(47) Dinh, H. Q.; Xu, L. Measuring the Similarity of Vector Fields Using Global Distributions. In *Lecture Notes in Computer Science (including subseries Lecture Notes in Artificial Intelligence and Lecture Notes in Bioinformatics)*; Springer, Berlin, Heidelberg, 2008; Vol. 5342 LNCS, pp 187–196. https://doi.org/10.1007/978-3-540-89689-0_23.

(48) Zhao, Y.; Truhlar, D. G. The M06 Suite of Density Functionals for Main Group Thermochemistry, Thermochemical Kinetics, Noncovalent Interactions, Excited States, and Transition Elements: Two New Functionals and Systematic Testing of Four M06-Class Functionals and 12 Other Function. *Theor. Chem. Acc.* **2008**, *120* (1–3), 215–241. https://doi.org/10.1007/s00214-007-0310-x.

(49) Ahlrichs, R.; Bär, M.; Häser, M.; Horn, H.; Kölmel, C. Electronic Structure Calculations on Workstation Computers: The Program System Turbomole. *Chem. Phys. Lett.* **1989**, *162* (3), 165–169. https://doi.org/10.1016/0009-2614(89)85118-8.

(50) Häser, M.; Ahlrichs, R. Improvements on the Direct SCF Method. *J. Comput. Chem.* **1989**, *10* (1), 104–111. https://doi.org/10.1002/jcc.540100111.

(51) Treutler, O.; Ahlrichs, R. Efficient Molecular Numerical Integration Schemes. *J. Chem. Phys.* **1995**, *102* (1), 346–354. https://doi.org/10.1063/1.469408.

(52) Eichkorn, K.; Weigend, F.; Treutler, O.; Ahlrichs, R. Auxiliary Basis Sets for Main Row Atoms and Transition Metals and Their Use to Approximate Coulomb Potentials. *Theor. Chem. Accounts Theory, Comput. Model. (Theoretica Chim. Acta)* **1997**, *97* (1–4), 119–124. https://doi.org/10.1007/s002140050244.

(53) Eichkorn, K.; Treutler, O.; Öhm, H.; Häser, M.; Ahlrichs, R. Auxiliary Basis Sets to Approximate Coulomb Potentials. *Chem. Phys. Lett.* **1995**, *240* (4), 283–290. https://doi.org/10.1016/0009-2614(95)00621-A.

(54) Weigend, F. Accurate Coulomb-Fitting Basis Sets for H to Rn. *Phys. Chem. Chem. Phys.* **2006**, *8* (9), 1057. https://doi.org/10.1039/b515623h.

(55) Sierka, M.; Hogekamp, A.; Ahlrichs, R. Fast Evaluation of the Coulomb Potential for Electron Densities Using Multipole Accelerated Resolution of Identity Approximation. *J. Chem. Phys.* **2003**, *118* (20), 9136–9148. https://doi.org/10.1063/1.1567253.

(56) Deglmann, P.; May, K.; Furche, F.; Ahlrichs, R. Nuclear Second Analytical Derivative Calculations Using Auxiliary Basis Set Expansions. *Chem. Phys. Lett.* **2004**, *384* (1–3),

103–107. https://doi.org/10.1016/j.cplett.2003.11.080.

(57) Von Arnim, M.; Ahlrichs, R. Performance of Parallel TURBOMOLE for Density Functional Calculations. *J. Comput. Chem.* **1998**, *19* (15), 1746–1757. https://doi.org/10.1002/(SICI)1096-987X(19981130)19:15<1746::AID-JCC7>3.0.CO;2-N.

(58) von Arnim, M.; Ahlrichs, R. Geometry Optimization in Generalized Natural Internal Coordinates. *J. Chem. Phys.* **1999**, *111* (20), 9183–9190. https://doi.org/10.1063/1.479510.

(59) Ahlrichs, R. Efficient Evaluation of Three-Center Two-Electron Integrals over Gaussian Functions. *Phys. Chem. Chem. Phys.* **2004**, *6* (22), 5119. https://doi.org/10.1039/b413539c.

(60) Klamt, A.; Schüürmann, G. COSMO: A New Approach to Dielectric Screening in Solvents with Explicit Expressions for the Screening Energy and Its Gradient. *J. Chem. Soc., Perkin Trans. 2* **1993**, *0* (5), 799–805. https://doi.org/10.1039/P29930000799.

(61) Sahakyan, A. B. Computational Studies of Dielectric Permittivity Effects on Chemical Shifts of Alanine Dipeptide. *Chem. Phys. Lett.* **2012**, *547*, 66–72. https://doi.org/10.1016/j.cplett.2012.07.069.

(62) Keith, T. A. AIMALL, TK Gristmill Software. *Overl. Park KS, USA,(aim. tkgristmill. com)* **2016**.

(63) Biegler-könig, F. W.; Bader, R. F. W.; Tang, T.-H. Calculation of the Average Properties of Atoms in Molecules. II. *J. Comput. Chem.* **1982**, *3* (3), 317–328. https://doi.org/10.1002/jcc.540030306.

(64) Keith, T. A. Computational Improvements for the Theory of Atoms in Molecules. *Chapter 4 Ph. D. Thesis Mol. Magn. Fields* **1993**, 176–213.

Graphical TOC Entry